Pergamon

Int. J. Heat Mass Transfer. Vol. 39, No. 17, pp. 3581–3594, 1996

0017-9310/96 $15.00 + 0.00

PII: S0017-9310(96)00042-7

The viscous stagnation-flow solidification problem

X. BIAN and R. H. RANGEL†

Department of Mechanical and Aerospace Engineering, University of California, Irvine, CA 92717, U.S.A.

(*Received* 7 *November* 1995 *and in final form* 30 *January* 1996)

Abstract—The viscous stagnation-flow solidification problem for a pure substance is investigated by means of quasi-steady, instantaneous-similarity, as well as finite-difference methods. The liquid velocity field, the solid and liquid temperature distributions, the solid–liquid interface location, as well as its growth rate, are obtained using all three methods and comparisons of the solutions are made. The instantaneous-similarity solution at a sufficiently small time is used as the initial field to start the finite-difference calculation. All three methods show the existence of an asymptotic limit of the solidification-front position. The effect on this limit of several important dimensionless parameters, including the Prandtl number, is presented.

1. INTRODUCTION

Heat transfer problems accompanied by phase change are of great interest in a wide range of natural processes and industrial applications such as in the metal, glass, plastic, and oil industries; preservation of food; cryosurgery; and others. Many analytical and numerical techniques have been reported for dealing with heat-diffusion-controlled freezing or melting problems since Stefan's classical study of the growth of sea ice [1], and early work on the problems of liquid–solid phase change was confined mainly to the cases in which the liquid melt is stagnant [2–4].

In addition to the studies of phase change in stagnant media, the need for a better understanding of the effect of the convection on the interface behavior and the solidification properties has been propelled by industrial demand such as the desire for more homogeneous semi-conductor crystals, the requirements in the nuclear industry, as well as a better understanding of natural ice formation. One of the distinctive features of the liquid–solid phase-changing process accompanied by fluid motion which introduces additional complications besides the basic nonlinearity of the transient phase-change problem, is that the location of the interface is influenced by the liquid motion in addition to the heat transfer to the interface. The problem of solid–liquid phase change in a flowing melt can be divided into three types: (a) phase change in external forced flow, (b) phase change in internal forced flow, and (c) phase change in natural-convection flow [5]. Examples of the studies on the convection effects on the phase-change process are those listed in refs. [6–11]. Lacroix has used a stream function-vorticity-temperature formulation to solve the melting problem that includes free convection [7]. A numerical study of three-dimensional natural convection during freezing of water has been made by Yeoh *et al.* [8]. Oldenburg and Spera have set up a hybrid model on the basis of the continuum model to study the phase change problem which involves convection [9].

One of the important engineering processes involving heat transfer accompanied by the solidification of liquid in motion is the metal spray forming process during which the high temperature liquid metal droplet deforms and solidifies during its impingment on a cold substrate. One way of approach to the study of the phase-change mechanism during the droplet deformation in such processes is to treat the melt and the solid as a continuum which may be represented in terms of enthalpy. The heat release during solidification is represented in terms of the appropriate enthalpy change [12]. The other way of approach is using the Neumann solution of the Stefan model to determine the liquid–solid interface location [13–16]. For the latter way of approach, a major shortcoming is that it does not take into account the effect of the liquid motion on the solidification behavior. Recently, a heat transfer and solidification model for the inviscid two-dimensional stagnation-flow was developed by Rangel and Bian [17, 18] to investigate the effect of liquid motion on its solidification behavior. This model provides some insight into the effect of the fluid motion on the solidification of a droplet impinging on a cold substrate in spray deposition.

The purpose of the present work is to study the effect of liquid motion on its solidification behavior in the case of a viscous two-dimensional stagnation flow. A stability analysis of the stagnation-flow solidification problem has been made by Brattkus and

† Author to whom correspondence should be addressed.

NOMENCLATURE

A	potential-flow strain rate
a	ratio of the liquid to solid thermal diffusivity (α_l/α_s)
b	ratio of the liquid to solid thermal conductivity (k_l/k_s)
c	specific heat
f	similarity stream function
$\tilde{f}$	nondimensional similarity stream function (f/L_v)
$\tilde{F}$	variable defined as $\tilde{F}(\tilde{Y},\tau)=\tilde{f}(\tilde{y},\tau)$
$\tilde{\tilde{F}}$	variable defined as $\tilde{\tilde{F}}(\eta,\tau)=\tilde{F}(\tilde{Y},\tau)$
g	variable defined as $\partial\tilde{f}/\partial\tilde{y}$
G	variable defined as $\partial\tilde{F}/\partial\tilde{Y}$
h_{sf}	latent heat of solidification
i	grid point in y' direction
I	total grid points in y' direction
k	thermal conductivity
L_v	characteristic length ($\sqrt{\nu/A}$)
L_α	characteristic length ($\sqrt{\alpha_s/A}$)
Pr	Prandtl number (ν/α_l)
q''	heat flux
s	solid phase thickness
$\tilde{s}_v$	nondimensional solid thickness (s/L_v)
$\tilde{s}_\alpha$	nondimensional solid thickness (s/L_α)
St	Stefan number $[c(T_m-T_0)/h_{sf}]$
T	temperature
t	time
t_c	characteristic time ($1/A$)
u	velocity component of liquid phase in the x-direction
v	velocity component of liquid phase in the y-direction
x	spatial coordinate parallel to the substrate
y	spatial coordinate normal to the substrate
$\tilde{y}$	nondimensional normal coordinate (y/L_v)
$\tilde{y}_\alpha$	nondimensional normal coordinate (y/L_α)
y'	transformed coordinate $[(2/\pi)\tan^{-1}(\tilde{y}/\tilde{s}_v)]$
$\tilde{Y}$	variable defined as $\tilde{y}-\tilde{s}_v(\tau)$.

Greek symbols

α	thermal diffusivity
η	similarity variable ($\tilde{y}/\sqrt{\tau}$)
θ	nondimensional temperature $[(T-T_m)/(T_m-T_0)]$
λ	solidification parameter
ν	kinematic viscosity of fluid
ρ	density
τ	nondimensional time (t/t_c).

Subscripts

i	initial
l	liquid phase
o	substrate
m	melting
p	iteration index
s	solid phase
v	dimensionless indication (with L_v as characteristic length)
α	dimensionless indication (with L_α as characteristic length).

Superscripts

~	nondimensional
n	discrete-time index.

Davis [19], who found that when Schmidt numbers are large, two-dimensional long-wave disturbances are unstable for any degree of constitutional undercooling. In our study, it is assumed that the physical properties are independent of temperature. The mathematical model of the viscous stagnation-flow solidification problem is set up by means of coupling the liquid-phase momentum equation and the conductive–convective liquid energy equation with the heat conduction equation in the solid region, as well as the energy balance equation at the interface. An instantaneous similarity method and a quasi-steady approximation are employed to solve the time-dependent system of equations. Furthermore, a finite-difference solution is obtained and compared with the two semi-analytical solutions. A parametric study of the effect of thermal and fluid properties such as the liquid phase Prandtl number, the Stefan number, the ratio of the initial liquid temperature and the cold substrate temperature, the ratio of the liquid and solid thermal conductivities, as well as the ratio of the liquid and solid thermal diffusivities on the solidification process is made. The liquid phase velocity and temperature distributions, and the solid phase temperature distribution, as well as the behavior of the solid–liquid interface location are investigated.

2. MATHEMATICAL FORMULATION

A schematic description of the half-space viscous stagnation-flow solidification problem is provided in Fig. 1. The fluid with temperature T_i higher than its melting temperature T_m flows towards a cold substrate which is maintained at a constant temperature T_0 lower than T_m. As a result, solidification occurs at the surface $y=0$ and the solid–liquid interface moves in

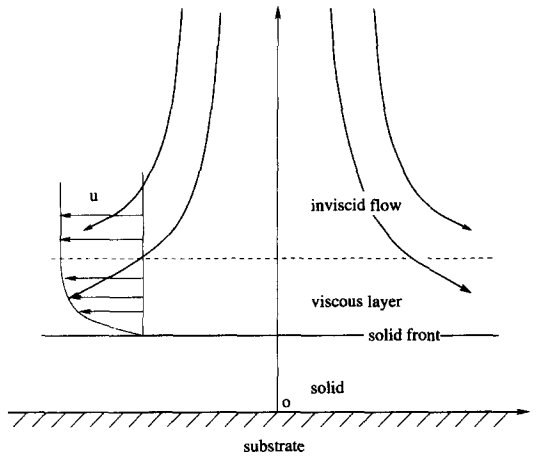

Fig. 1. Solidification in a half space: the viscous stagnation-flow solidification problem.

the positive normal direction. The liquid-phase flow field is an unsteady stagnation-flow with a zero-velocity moving boundary. Viscous dissipation is neglected, thus rendering the thermal problem one-dimensional.

The set of equations for this viscous stagnation-flow solidification problem is established as follows.

The energy equation for the solid phase is

$$\frac{\partial^2 T_s}{\partial y^2} = \frac{1}{\alpha_s}\frac{\partial T_s}{\partial t} \quad \text{in } 0 < y < s(t), t > 0 \tag{1}$$

with the boundary conditions: $T_s(0,t) = T_0$ and $T_s(s,t) = T_m$.

The continuity and momentum equations of the liquid phase are

$$\frac{\partial u}{\partial x} + \frac{\partial v}{\partial y} = 0 \tag{2}$$

$$\frac{\partial u}{\partial t} + u\frac{\partial u}{\partial x} + v\frac{\partial u}{\partial y} = -\frac{1}{\rho}\frac{\partial p}{\partial x} + \nu\left(\frac{\partial^2 u}{\partial x^2} + \frac{\partial^2 u}{\partial y^2}\right) \tag{3}$$

$$\frac{\partial v}{\partial t} + u\frac{\partial v}{\partial x} + v\frac{\partial v}{\partial y} = -\frac{1}{\rho}\frac{\partial p}{\partial y} + \nu\left(\frac{\partial^2 v}{\partial x^2} + \frac{\partial^2 v}{\partial y^2}\right) \tag{4}$$

with the boundary conditions: $u = v = 0$ at $y = s(t)$. Furthermore, as $y \to \infty$, the liquid phase velocity field u, v must approach the inviscid stagnation-flow solution:

$$u = Ax, \quad v = -A(y - s(t)). \tag{5}$$

Neglecting viscous dissipation, the energy equation for the liquid phase is

$$\frac{\partial T_l}{\partial t} + u\frac{\partial T_l}{\partial x} + v\frac{\partial T_l}{\partial y} = \alpha_l\left[\frac{\partial^2 T_l}{\partial x^2} + \frac{\partial^2 T_l}{\partial y^2}\right]. \tag{6}$$

In analogy to the velocity distribution of the steady stagnation-flow problem, the viscous liquid-phase velocity field is assumed to be the following:

$$u = Axf'(t,y), \quad v = -Af(t,y), \tag{7}$$

where $f' = \partial f/\partial y$.

Substituting the above expressions for u and v into the momentum equations, we get

$$\frac{\partial f'}{\partial t} + Af'^2 - Aff'' = A + \nu f''' \tag{8}$$

with the boundary conditions: $f'(s,t) = 0, f(s,t) = 0$, and $f'(\infty,t) = 1$.

For uniform interface temperature, the liquid thermal problem is one-dimensional, and the liquid-phase energy equation can be simplified to

$$\frac{\partial T_l}{\partial t} - Af(t,y)\frac{\partial T_l}{\partial y} = \alpha_l\frac{\partial^2 T_l}{\partial y^2}. \tag{9}$$

The energy balance equation at the interface $y = s(t)$ is

$$k_s\frac{\partial T_s}{\partial y} - k_l\frac{\partial T_l}{\partial y} = \rho h_{sf}\frac{\mathrm{d}s(t)}{\mathrm{d}t}. \tag{10}$$

Introducing the dimensionless temperature θ, dimensionless coordinate $\tilde{y}$, and dimensionless time τ, the set of equations [(1), (8), (9) and (10)] is rewritten as:

solid-phase energy equation [equation (1)]

$$\frac{\partial \theta_s}{\partial \tau} = \frac{1}{aPr}\frac{\partial^2 \theta_s}{\partial \tilde{y}^2} \quad \text{in } 0 < \tilde{y} < \tilde{s}_v(\tau), \tau > 0 \tag{11}$$

with boundary conditions: $\theta_s(0,\tau) = -1$ and $\theta_s(\tilde{s}_v,\tau) = 0$;

liquid-phase momentum equation [equation (8)],

$$\frac{\partial \tilde{f}'}{\partial \tau} + \tilde{f}'^2 - \tilde{f}\tilde{f}'' = 1 + \tilde{f}''' \tag{12}$$

with boundary conditions: $\tilde{f}'(\tilde{s}_v,\tau) = 0$, $\tilde{f}(\tilde{s}_v,\tau) = 0$, and $\tilde{f}'(\infty,\tau) = 1$, where $\tilde{f}' = \partial\tilde{f}/\partial\tilde{y}$; liquid-phase energy equation [equation (9)],

$$\frac{\partial \theta_l}{\partial \tau} - \tilde{f}\frac{\partial \theta_l}{\partial \tilde{y}} = \frac{1}{Pr}\frac{\partial^2 \theta_l}{\partial \tilde{y}^2} \tag{13}$$

with boundary conditions: $\theta_l(\tilde{s}_v,\tau) = 0$ and $\theta_l(\infty,\tau) = \theta_i$.

The energy balance at the interface $\tilde{y} = \tilde{s}_v$ [equation (10)] becomes

$$\frac{\partial \theta_s}{\partial \tilde{y}} - b\frac{\partial \theta_l}{\partial \tilde{y}} = \frac{aPr}{St}\frac{\mathrm{d}\tilde{s}_v}{\mathrm{d}\tau}. \tag{14}$$

3. QUASI-STEADY SOLUTION

The Neumann solution of the classical Stefan problem [20] shows that the growth rate of the solid front is proportional to the square root of time, hence the velocity of the solidification front approaches zero as time approaches infinity. A similar behavior is expected in the convective solidification problem. Therefore, a quasi-steady solution is expected for large

values of times. The quasi-steady approximation is applied by neglecting the time derivative in the governing equations. The boundary and initial conditions remain unchanged.

The solid-phase energy equation becomes

$$\frac{\partial^2\theta_s}{\partial\tilde{y}^2}=0 \tag{15}$$

with the solution

$$\theta_s=\frac{\tilde{y}}{\tilde{s}_v(\tau)}-1. \tag{16}$$

Now let $\tilde{f}(\tilde{y},\tau)=\tilde{F}(\tilde{y},\tau)$, where $\tilde{Y}=\tilde{y}-\tilde{s}_v(\tau)$, so that the liquid-phase momentum equation [12] can be rewritten as

$$\frac{\partial\tilde{F}'}{\partial\tau}-\tilde{F}''\frac{\mathrm{d}\tilde{s}_v}{\mathrm{d}\tau}+\tilde{F}'^2-\tilde{F}\tilde{F}''=1+\tilde{F}''' \tag{17}$$

with boundary conditions: $\tilde{F}'(0,\tau)=\tilde{F}(0,\tau)=0$ and $\tilde{F}'(\infty,\tau)=1$, where $\tilde{F}'=\partial\tilde{F}/\partial\tilde{Y}$.

Invoking the quasi-steady assumption, equation (17) is simplified to

$$\tilde{F}'^2-\tilde{F}\tilde{F}''=1+\tilde{F}''' \tag{18}$$

with boundary conditions: $\tilde{F}'(0)=\tilde{F}(0)=0$ and $\tilde{F}(\infty)=1$. This is recognized as the steady plane stagnation-flow equation [21].

Similarly, the liquid-phase energy equation becomes

$$-\tilde{f}\frac{\partial\theta_l}{\partial\tilde{y}}=\frac{1}{Pr}\frac{\partial^2\theta_l}{\partial\tilde{y}^2}. \tag{19}$$

The solution of equation (19) is

$$\theta_l=\theta_i\frac{\displaystyle\int_{\tilde{s}_v}^{\tilde{y}}\exp\left[-Pr\int_{\tilde{s}_v}^{y'}\tilde{f}\,\mathrm{d}y''\right]\mathrm{d}y'}{\displaystyle\int_{\tilde{s}_v}^{\infty}\exp\left[-Pr\int_{\tilde{s}_v}^{y'}\tilde{f}\,\mathrm{d}y''\right]\mathrm{d}y'} \tag{20}$$

or alternatively

$$\theta_l=\theta_i\frac{\displaystyle\int_0^{\tilde{Y}}\exp\left[-Pr\int_0^{Y'}\tilde{F}\,\mathrm{d}Y''\right]\mathrm{d}Y'}{\displaystyle\int_0^{\infty}\exp\left[-Pr\int_0^{Y'}\tilde{F}\,\mathrm{d}Y''\right]\mathrm{d}Y'}, \tag{21}$$

where $\tilde{F}(\tilde{y},\tau)$ is the quasi-steady solution of the momentum equation (12), that is, the solution of equation (18). Using the solutions of the solid- and liquid-phase energy equations, the interface energy balance [equation (14)] can be written as

$$\frac{aPr}{St}\frac{\mathrm{d}\tilde{s}_v}{\mathrm{d}\tilde{\tau}}=\frac{1}{\tilde{s}_v}-\frac{\theta_i b}{\displaystyle\int_0^{\infty}\exp\left[-Pr\int_0^{y'}\tilde{F}\,\mathrm{d}y''\right]\mathrm{d}y'}. \tag{22}$$

The asymptotic value of $\tilde{s}_v$ can now be obtained by using the fact that $\mathrm{d}\tilde{s}_v/\mathrm{d}\tau\to 0$ as $\tau\to\infty$. Then equation (22) gives

$$\tilde{s}_v\to\tilde{s}_{v\max}=\frac{\displaystyle\int_0^{\infty}\exp\left[-Pr\int_0^{y'}\tilde{F}\,\mathrm{d}y''\right]\mathrm{d}y'}{\theta_i b}\quad\text{as }\tau\to\infty. \tag{23}$$

Integrating equation (22) and using the result of equation (23) yields

$$\tau=-\frac{aPr\tilde{s}_{v\max}}{St}\left[\tilde{s}_{v\max}\ln\left(1-\frac{\tilde{s}_v}{\tilde{s}_{v\max}}\right)+\tilde{s}_v\right]. \tag{24}$$

It can be seen from equation (23) that there exits an upper limit of the solid phase thickness as time goes to infinity. This result is consistent with the analysis of the inviscid stagnation-flow solidification problem [17, 18], indicating a significant difference between the stagnation-flow solidification problem and the classical solidification problem.

As the location of the solid front approaches a quasi-steady behavior, the heat flux on the liquid side of the interface approaches a finite value. At the interface, the heat flux on the solid side continues to decrease as the solid front advances. When the solid-phase heat flux equals the finite liquid-phase value, no further solidification is possible. Since the asymptotic value of the solid-front location is determined by heat transfer in the absence of solidification (or when solidification ceases), it is not surprising that it is independent of the Stefan number. Further discussion of this behavior will be made in Section 7.4.

4. FINITE-DIFFERENCE SOLUTION OF THE LIQUID-PHASE MOMENTUM EQUATION

The momentum equation (12) may be solved numerically in its transformed form [equation (17)] by introducing a new variable $G=\tilde{F}'(\tilde{Y},\tau)=\partial\tilde{F}/\partial\tilde{Y}$ so that equation (12) is transformed into the following two coupled equations:

$$\frac{\partial G}{\partial\tau}=\frac{\partial^2 G}{\partial\tilde{Y}^2}+\left(\frac{\mathrm{d}\tilde{s}_v}{\mathrm{d}\tau}+\tilde{F}\right)\frac{\partial G}{\partial\tilde{Y}}+1-G^2 \tag{25}$$

$$G=\frac{\partial\tilde{F}}{\partial\tilde{Y}} \tag{26}$$

with the corresponding boundary conditions: $F(\tau,0)=0$, $G(\tau,0)=0$ and $G(\tau,\infty)=1$. The initial velocity field of the liquid phase is chosen as the solution of the steady plane stagnation-flow equation [21],

$$\tilde{F}'^2-\tilde{F}\tilde{F}''=1+\tilde{F}'''. \tag{27}$$

Equation (25) is rewritten into finite-difference form by applying the Crank–Nicolson method, and the resulting algebraic system of equations can be solved

with the TDMA method [22]. Equation (26) is solved with the modified Euler method.

5. INSTANTANEOUS-SIMILARITY SOLUTION OF THE ENERGY EQUATIONS

In this section, the instantaneous-similarity method is applied to solve the energy equations of the solid and liquid phases (11) and (13), as well as the interface energy balance equation (14), while the momentum equation of the liquid phase (12) is solved by the finite-difference method described above.

Introducing a similarity variable η, the governing equations [equations (11), (13), (14)] are transformed to:

Solid-phase energy equation [equation (11)]

$$\tau\frac{\partial\theta_s}{\partial\tau}=\frac{1}{aPr}\frac{\partial^2\theta_s}{\partial\eta^2}+\frac{1}{2}\eta\frac{\partial\theta_s}{\partial\eta} \tag{28}$$

with boundary conditions: $\theta_s(0,\tau)=-1$ and $\theta_s(\lambda_v,\tau)=0$, where $\lambda_v=\tilde{s}_v(\tau)/\sqrt{\tau}$ is in general a function of τ. Note that in the classical Stefan solidification problem, $s(t)$ is proportional to $\sqrt{t}$ so that the parameter λ is equal to a constant in that case.

Liquid-phase energy equation [equation (13)]

$$\tau\frac{\partial\theta_l}{\partial\tau}=\left[\tilde{\mathscr{F}}(\eta,\tau)\tau^{1/2}+\frac{1}{2}\eta\right]\frac{\partial\theta_l}{\partial\eta}+\frac{1}{Pr}\frac{\partial^2\theta_l}{\partial\eta^2}, \tag{29}$$

where $\tilde{\mathscr{F}}(\eta,\tau)=\tilde{F}(\tilde{Y},\tau)=\tilde{f}(\tilde{y},t)$ and with boundary conditions: $\theta_l(\lambda_v,\tau)=0$ and $\theta_l(\infty,\tau)=\theta_i$;

The energy balance at the interface location [equation (14)] becomes

$$\frac{\partial\theta_s}{\partial\eta}-b\frac{\partial\theta_l}{\partial\eta}=\frac{1}{2}\frac{aPr}{St}\lambda_v+\frac{aPr}{St}\tau\frac{d\lambda_v}{d\tau}\quad\text{at }\eta=\lambda_v. \tag{30}$$

In accordance with the instantaneous similarity assumptions, we neglect terms involving derivatives with respect to τ and integrate the resulting ordinary differential equations. The results are expected to be valid for small values of τ, but as will be shown below, they are also valid for large values of τ.

The solid-phase temperature distribution is

$$\theta_s=-1+\frac{\operatorname{erf}(\frac{1}{2}\sqrt{aPr}\eta)}{\operatorname{erf}(\frac{1}{2}\sqrt{aPr}\lambda_v)}, \tag{31}$$

while the liquid-phase temperature distribution is

$$\theta_l=\theta_i\frac{\displaystyle\int_{\lambda_v}^{\eta}\exp\left[-\frac{Pr}{4}\eta'^2-Pr\tau^{1/2}\int_{\lambda_v}^{\eta'}\tilde{\mathscr{F}}(\eta'',\tau)\,d\eta''\right]d\eta'}{\displaystyle\int_{\lambda_v}^{\infty}\exp\left[-\frac{Pr}{4}\eta'^2-Pr\tau^{1/2}\int_{\lambda_v}^{\eta'}\tilde{\mathscr{F}}(\eta'',\tau)\,d\eta''\right]d\eta'}. \tag{32}$$

The interface energy balance equation becomes

$$\sqrt{\frac{aPr}{\pi}}\frac{\exp(-\frac{1}{4}aPr\lambda_v^2)}{\operatorname{erf}(\frac{1}{2}\sqrt{aPr}\lambda_v)}-\frac{aPr}{2St}\lambda_v-\frac{b\theta_i\exp[-\frac{1}{4}Pr\lambda_v^2]}{\displaystyle\int_{\lambda_v}^{\infty}\exp\left[-\frac{Pr}{4}\eta'^2-Pr\tau^{1/2}\int_{\lambda_v}^{\eta'}\tilde{\mathscr{F}}(\eta'',\tau)\,d\eta''\right]d\eta'}=0 \tag{33}$$

from which λ_v can be determined. Equation (33) shows that λ_v is a function of time, in contrast with the λ_v of the classical Stefan problem which is independent of time. By coupling the solution of equations (25) and (26) with the solution of equation (33), the root of equation (33), λ_v, is obtained by iteration at each time.

6. NUMERICAL SOLUTION BY FINITE-DIFFERENCE METHOD

The set of governing equations consists of the solid-phase energy equation [equation (11)], the liquid-phase momentum equation [equation (12)], the liquid-phase energy equation [equation (13)], and the interface energy-balance equation [equation (14)].

Introducing the following transformation:

$$y'=\frac{2}{\pi}\tan^{-1}\left(\frac{\tilde{y}}{\tilde{s}_v}\right) \tag{34}$$

the coordinates $(\tilde{y},\tau)$ are transformed into a new coordinate system (y',τ), so that the semi-infinite domain is transformed into a finite domain and the moving-interface problem is converted into a fixed boundary problem.

The solid-phase energy equation [equation (11)] is transformed to

$$\frac{\partial\theta_s}{\partial\tau}=\frac{1}{aPr}\frac{4}{\pi^2}\cos^4\left(\frac{\pi}{2}y'\right)\frac{1}{\tilde{s}_v^2}\frac{\partial^2\theta_s}{\partial y'^2}+\left[\frac{1}{\pi}\sin(\pi y')\frac{1}{\tilde{s}_v}\frac{d\tilde{s}_v}{d\tau}-\frac{1}{aPr}\frac{2}{\pi}\sin(\pi y')\cos^2\left(\frac{\pi}{2}y'\right)\frac{1}{\tilde{s}_v^2}\right]\frac{\partial\theta_s}{\partial y'}$$

$$\text{for } 0<y'<0.5 \tag{35}$$

with boundary conditions: $\theta_s=-1$ at $\tilde{y}=0$, and $\theta_s=0$ at $\tilde{y}=0.5$.

Introducing the variable $g=\partial\tilde{f}/\partial\tilde{y}$, the liquid phase momentum equation [equation (12)] can be rewritten as the following two coupled equations:

$$\frac{\partial g}{\partial\tau}=\frac{\partial^2 g}{\partial\tilde{y}^2}+\tilde{f}\frac{\partial g}{\partial\tilde{y}}+1-g^2,\quad g=\frac{\partial\tilde{f}}{\partial\tilde{y}} \tag{36}$$

with boundary conditions: $\tilde{f}=0$ and $g=0$ at $\tilde{y}=\tilde{s}_v$, and $g\to 1$ as $\tilde{y}\to\infty$.

The transformed liquid phase momentum equations are

$$\frac{\partial g}{\partial \tau} = \frac{4}{\pi^2}\cos^4\left(\frac{\pi}{2}y'\right)\frac{1}{\tilde{s}_v^2}\frac{\partial^2 g}{\partial y'^2} + \left[\frac{1}{\pi}\sin(\pi y')\frac{1}{\tilde{s}_v}\frac{d\tilde{s}_v}{d\tau} - \frac{2}{\pi}\sin(\pi y') \times \cos^2\left(\frac{\pi}{2}y'\right)\frac{1}{\tilde{s}_v^2} + \frac{2}{\pi}\tilde{f}\cos^2\left(\frac{\pi}{2}y'\right)\frac{1}{\tilde{s}_v}\right]\frac{\partial g}{\partial y'} + 1 - g^2$$

$$\text{for } 0.5 < y' < 1 \tag{37}$$

and

$$g = \frac{2}{\pi}\cos^2\left(\frac{\pi}{2}y'\right)\frac{1}{\tilde{s}_v}\frac{\partial \tilde{f}}{\partial y'} \tag{38}$$

with boundary conditions: $\tilde{f} = 0$ and $g = 0$ at $y' = 0.5$, and $g = 1$ at $y' = 1$.

The liquid-phase energy equation [equation (13)] is transformed to

$$\frac{\partial \theta_l}{\partial \tau} = \frac{1}{Pr}\frac{4}{\pi^2}\cos^4\left(\frac{\pi}{2}y'\right)\frac{1}{\tilde{s}_v^2}\frac{\partial^2 \theta_l}{\partial y'^2} + \left[\frac{1}{\pi}\sin(\pi y')\frac{1}{\tilde{s}_v}\frac{d\tilde{s}_v}{d\tau} - \frac{1}{Pr}\frac{2}{\pi}\sin(\pi y') \times \cos^2\left(\frac{\pi}{2}y'\right)\frac{1}{\tilde{s}_v^2} + \frac{2}{\pi}\tilde{f}\cos^2\left(\frac{\pi}{2}y'\right)\frac{1}{\tilde{s}_v}\right]\frac{\partial \theta_l}{\partial y'}$$

$$\text{for } 0.5 < y' < 1 \tag{39}$$

with boundary conditions: $\theta_l = 0$ at $y' = 0.5$, and $\theta_l = \theta_i$ at $y' = 1$.

Finally, the interface energy equation [equation (14)] is transformed to

$$\frac{\partial \theta_s}{\partial y'} - b\frac{\partial \theta_l}{\partial y'} = \frac{aPr}{St}\pi\tilde{s}_v\frac{d\tilde{s}_v}{d\tau}. \tag{40}$$

By applying the Crank–Nicolson method, equations (35), (37) and (39) can be written in finite-difference form and can be solved with standard techniques.

7. RESULTS AND DISCUSSION

In this section, the temperature distributions in both the solid and liquid phases as well as the time evolution of the interface location obtained from the quasi-steady solution, the instantaneous-similarity method as well as the finite-difference method are displayed, and comparisons between the three methods are made. In addition, parametric studies are made to demonstrate the effect of the Prandtl and Stefan numbers and the dimensionless ratios θ_i, a, and b on the solidification behavior. In all the figures, $L_\alpha = \sqrt{\alpha_s/A}$ is used as the length scale to nondimensionalize the interface location s and the normal coordinate y.

7.1. *Evaluation of the instantaneous-similarity method*

An estimate of the accuracy of the instantaneous-similarity method is obtained by calculating the magnitude of the term $\tau(\partial\theta/\partial\tau)$ for the solid phase. From the solution of the solid phase temperature [equation (31)], we obtain

$$\frac{\partial \theta_s}{\partial \tau} = -\frac{\operatorname{erf}(\sqrt{aPr}\eta/2)\exp(-aPr\lambda_v^2/4)\sqrt{aPr}/\pi}{(\operatorname{erf}(\sqrt{aPr}\lambda_v/2))^2}\frac{\partial \lambda_v}{\partial \tau}. \tag{41}$$

The maximum value of $\partial\theta_s/\partial\tau$ is at $\eta = \lambda_v$, where

$$\left.\frac{\partial \theta_s}{\partial \tau}\right|_{\eta=\lambda_v} = -\frac{\sqrt{aPr}/\pi\exp(-aPr\lambda_v^2/4)}{\operatorname{erf}(\sqrt{aPr}\lambda_v/2)}\frac{\partial \lambda_v}{\partial \tau}. \tag{42}$$

It can be shown that during the initial stages of solidification, the value of $\tau(\partial\theta_s/\partial\tau)|_{\eta=\lambda_v}$ is small enough to ensure the accuracy of the instantaneous-similarity solution.

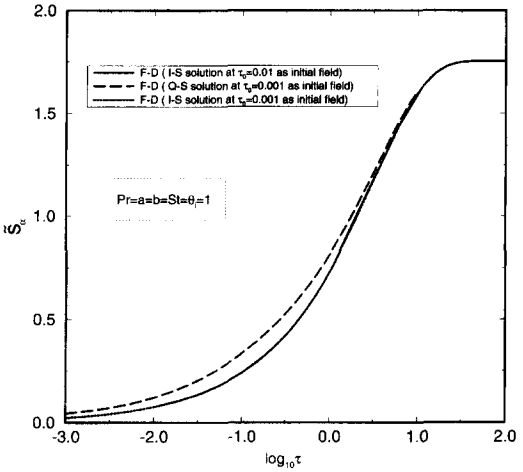

Fig. 2. Effect of the starting time on the finite-difference solution: solidification front vs time.

7.2. *Numerical considerations for the finite-difference method*

The system of equations (35)–(40) has a singularity at $\tau = 0$ ($\tilde{s} = 0$). Therefore, the finite-difference solution cannot be started at $\tau = 0$, but instead must be initiated at some sufficiently-small time $\tau = \tau_0$. It has been shown in the previous section that the instantaneous-similarity solution yields the correct limiting form of the solution for $\tau \to 0$.

In Fig. 2, a comparison of the dimensionless solid-front time evolution obtained with the finite-difference method starting from different initial fields is made. For comparison purposes, the finite-difference solution uses both the instantaneous-similarity and the quasi-steady solutions as the initial fields. It can be observed that the three solutions approach the same upper limit as time becomes very large. The finite-difference solution which starts from the quasi-steady initial field gradually evolves towards the finite-difference solution which uses the instantaneous-similarity solution as the initial field. This demonstrates that the finite-difference solution converges to the cor-

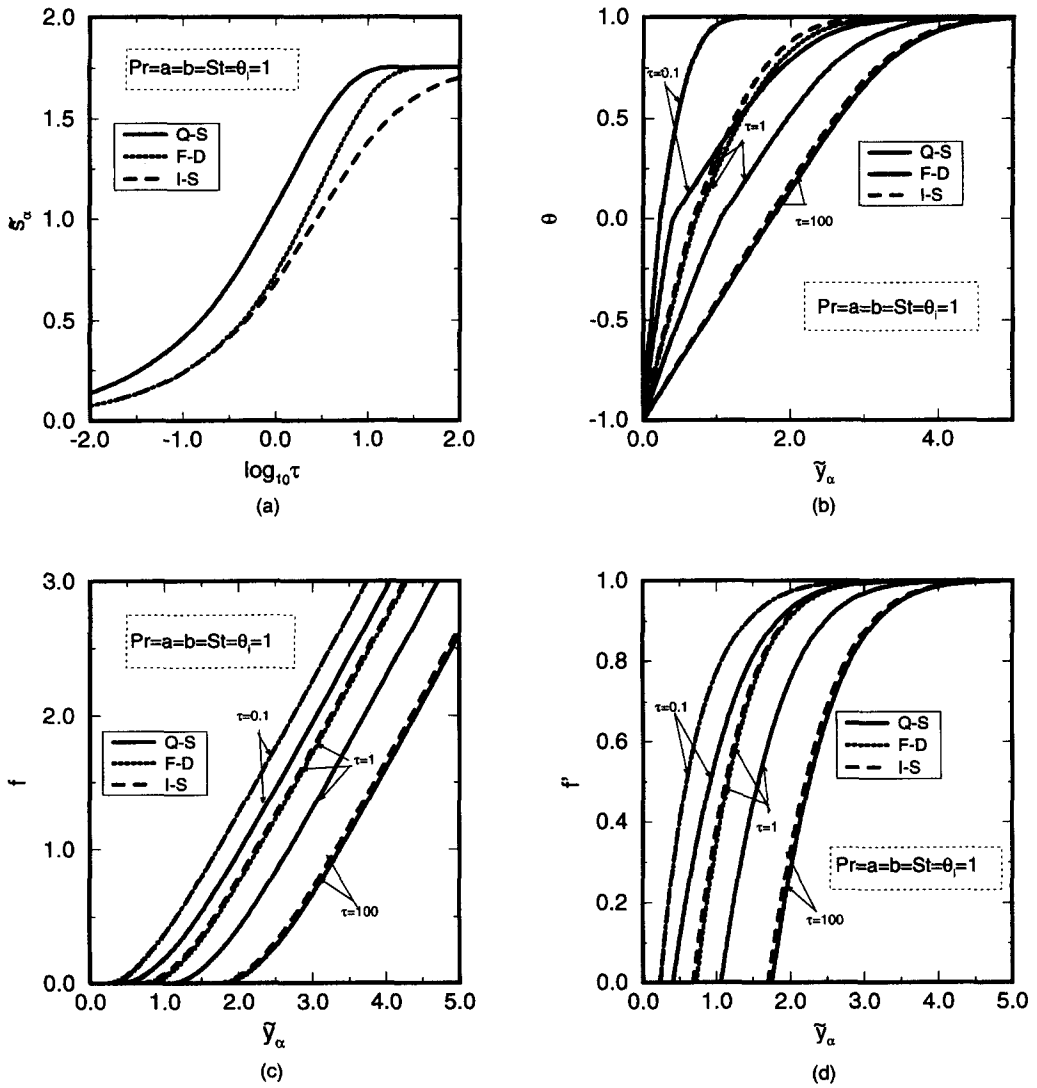

Fig. 3. Comparison of the solidification behavior obtained with different methods: (a) solid-front evolution vs time; (b) temperature distributions; (c) velocity distributions; (d) velocity gradient distributions.

rect long-time behavior, even if it is started with an inaccurate initial condition, such as the one obtained from the quasi-steady solution. It can also be seen that using the instantaneous-similarity solution at either $\tau_0 = 0.001$ or $\tau_0 = 0.01$ as the initial field for the finite-difference method makes no significant difference in the solution of the solid-front location. Thus we can conclude that $\tau_0 = 0.01$ is an appropriate small time to ensure the accuracy of the finite-difference solution at later times. In the following parametric study, all the finite-difference solutions are initiated at $\tau_0 = 0.01$ from the instantaneous-similarity solution.

7.3. *Comparison of the methods*

Figure 3 provides a comparison of the solidification behavior obtained with the three methods of solution for the case of $Pr = a = b = \theta_i = St = 1$. In Fig. 3(a), a comparison of the time evolution of the dimensionless solid-front location $\tilde{s}_\alpha$ obtained with the three methods is made. The finite-difference solution is taken as the *exact* solution. It can be observed that in comparison to the finite-difference method, the quasi-steady method overpredicts the solidification rate, while the instantaneous-similarity method underpredicts it. It can also be observed that the three solutions approach the same upper limit as time becomes very large. Figure 3(b) shows a comparison of the predicted temperature distributions. During the initial stages of solidification ($\tau = 0.1$), the numerical solution is much closer to the instantaneous-similarity solution than to the quasi-steady solution, which yields an accurate description of the solidification behavior only for very large times. The instantaneous-similarity solution is accurate for small times, as demonstrated before. At $\tau = 1$, the numerical solution lies between the solution obtained with the two analytical

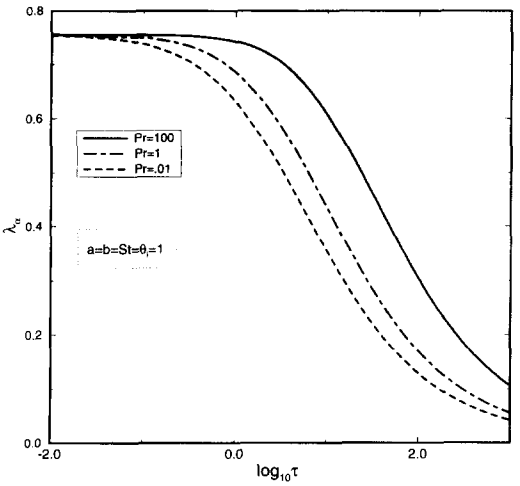

Fig. 4. Instantaneous-similarity solution: variation of λ with time; effect of Pr.

methods. Again expectedly, as time becomes very large ($\tau = 100$), the three solutions converge to the same result, with the instantaneous-similarity method lagging slightly behind. The corresponding fluid behavior is shown in Fig. 3(c, d). Figure 3(c) shows the normal-velocity distribution obtained from the three methods at different stages of solidification, while the corresponding normal-velocity gradient profile is shown in Fig. 3(d). In the early stages of solidification ($\tau = 0.1$), both the finite-difference and the instantaneous-similarity solutions yield an accurate description of the liquid-phase velocity distribution, with the quasi-steady solution overpredicting the growth. At the intermediate stages of solidification ($\tau = 1$), the instantaneous-similarity solution tends to lag behind the finite-difference solution. At the late stages of solidification ($\tau = 100$), both the quasi-steady and the finite-difference solutions provide an accurate description of the fluid motion, with the instantaneous-similarity solution lagging slightly behind. As time goes to infinity, all three methods yield the same result.

7.4. *Parametric studies*

This section contains solidification results for different fluids and thermal properties to demonstrate the effect of the Prandtl number, the Stefan number and the dimensionless ratios θ_i, a and b.

7.4.1. *Effect of* Pr *number*. Figure 4 shows the instantaneous-similarity solution of the variation of λ_α with τ for different values of Pr for the case of $\theta_i = a = b = 1$. It should be noted that λ_α approaches 0 as τ approaches infinity and λ_α decreases faster for smaller values of the Prandtl number.

Moreover, for a fixed value of τ, a larger value of the Prandtl number corresponds to a higher value of λ_α, and hence a larger value of $\tilde{s}_\alpha$. Notice that the length scale in all the figures is L_α, hence the real value of solid thickness is $s = \tilde{s}_\alpha\sqrt{\alpha_s/A} = \tilde{s}_\alpha\sqrt{\nu/(aPrA)}$. For a chosen value of τ, if we compare the case of $Pr = 0.01$ with that of $Pr = 100$, it can be seen that although the value of λ_α for the case of $Pr = 0.01$ is smaller than that for the latter case, the dimensional value of the solid-front location s will be much larger for the former case.

Figure 5 shows the evolution of the dimensionless solid front $\tilde{s}_\alpha$ with time for three different Prandtl numbers obtained with the quasi-steady and the instantaneous-similarity method. It can be seen that the dimensionless solid front grows faster for higher Pr number. Moreover, the dimensionless solid front location approaches an upper limit as time becomes very large. This dimensionless upper limit is larger for higher Pr number. Again note that, as explained in the discussion of Fig. 4, the corresponding value of the dimensional solid-front location and its upper limit are higher for the fluid with smaller Pr.

Figure 6 shows the dependence of the dimensionless solid-front upper limit location on the Prandtl number for the case of (1) $\theta_i = a = b = 1$, (2) $\theta_i = 1$,

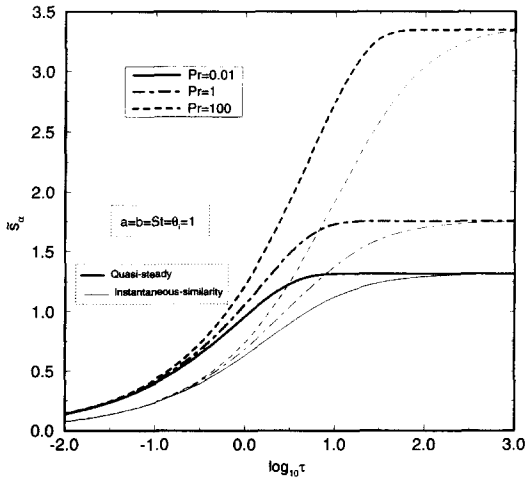

Fig. 5. Quasi-steady and instantaneous-similarity solutions of the solid front location vs time for different Pr.

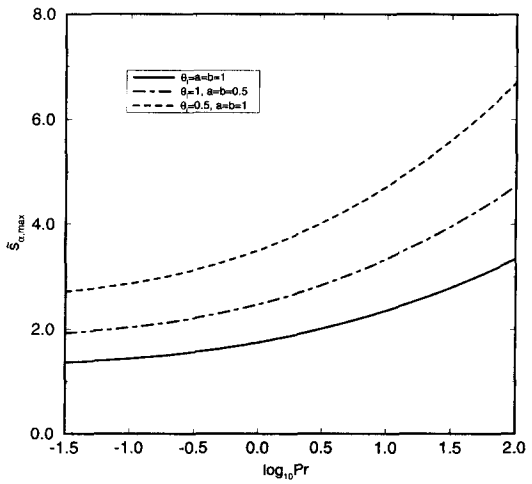

Fig. 6. Variation of the upper limit of the solid-front location with Pr.

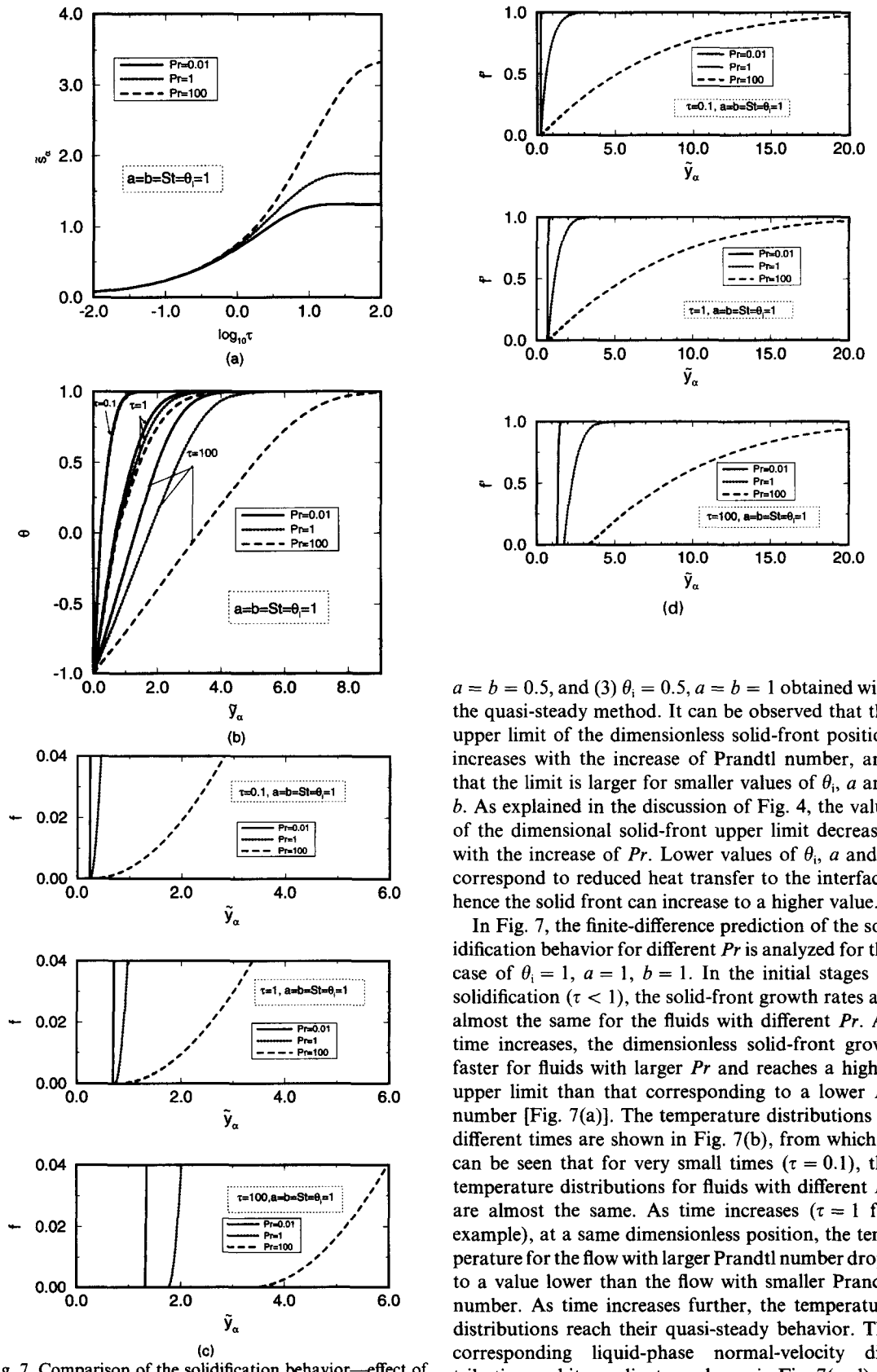

Fig. 7. Comparison of the solidification behavior—effect of Prandtl number: (a) solid-front evolution vs time; (b) temperature distributions; (c) velocity distributions; (d) velocity gradient distributions.

$a = b = 0.5$, and (3) $\theta_i = 0.5$, $a = b = 1$ obtained with the quasi-steady method. It can be observed that the upper limit of the dimensionless solid-front position increases with the increase of Prandtl number, and that the limit is larger for smaller values of θ_i, a and b. As explained in the discussion of Fig. 4, the value of the dimensional solid-front upper limit decreases with the increase of Pr. Lower values of θ_i, a and b correspond to reduced heat transfer to the interface, hence the solid front can increase to a higher value.

In Fig. 7, the finite-difference prediction of the solidification behavior for different Pr is analyzed for the case of $\theta_i = 1$, $a = 1$, $b = 1$. In the initial stages of solidification ($\tau < 1$), the solid-front growth rates are almost the same for the fluids with different Pr. As time increases, the dimensionless solid-front grows faster for fluids with larger Pr and reaches a higher upper limit than that corresponding to a lower Pr number [Fig. 7(a)]. The temperature distributions at different times are shown in Fig. 7(b), from which it can be seen that for very small times ($\tau = 0.1$), the temperature distributions for fluids with different Pr are almost the same. As time increases ($\tau = 1$ for example), at a same dimensionless position, the temperature for the flow with larger Prandtl number drops to a value lower than the flow with smaller Prandtl number. As time increases further, the temperature distributions reach their quasi-steady behavior. The corresponding liquid-phase normal-velocity distribution and its gradient are shown in Fig. 7(c, d). It can be observed that along the dimensionless normal direction $\tilde{y}_\alpha$, the gradient of the normal velocity for

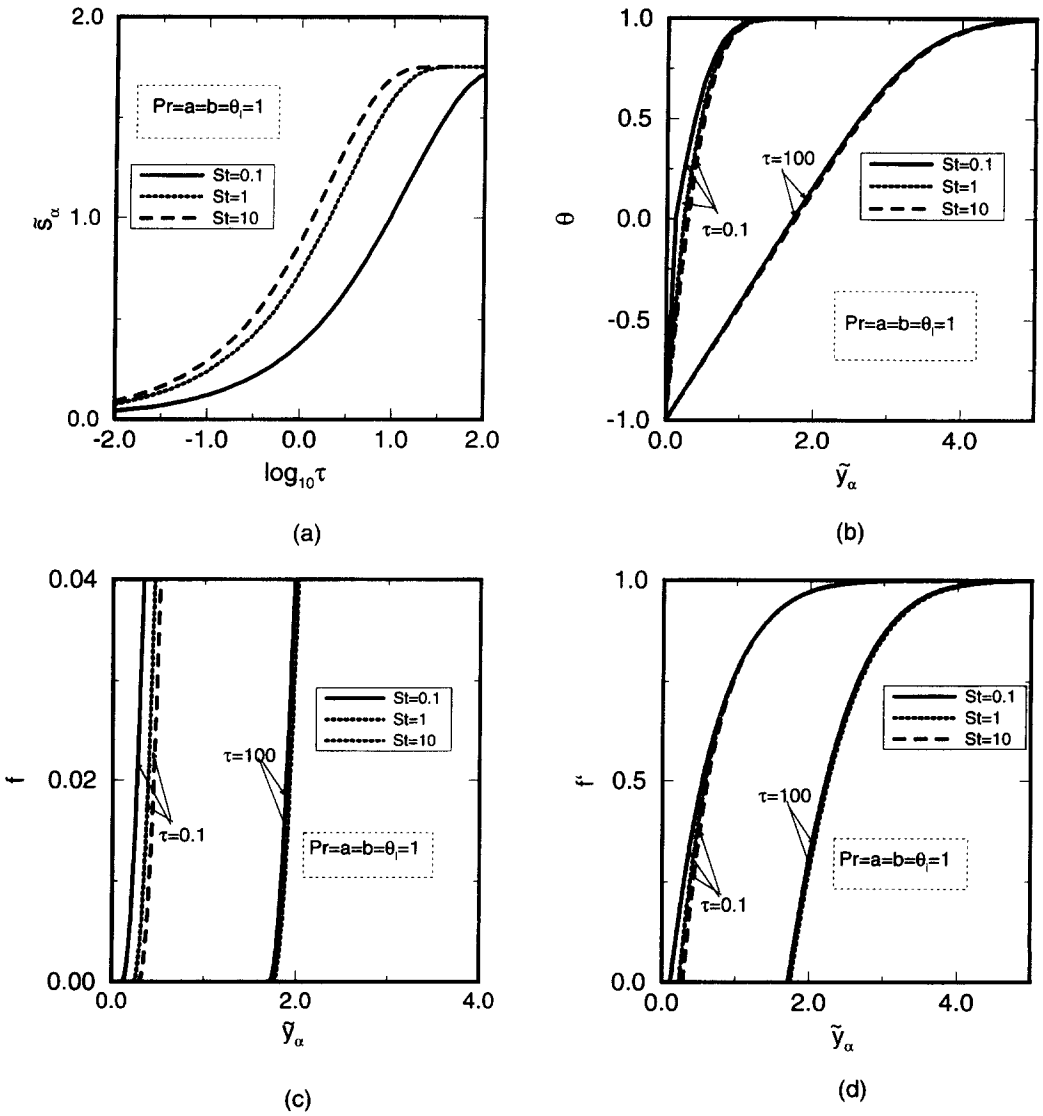

Fig. 8. Comparison of the solidification behavior—effect of Stefan number: (a) solid-front evolution vs time; (b) temperature distributions; (c) velocity distributions; (d) velocity gradient distributions.

the fluid with large Pr (100) increases much slower than that for the fluid with smaller Pr (0.01). The normal velocity increases more rapidly along the dimensionless normal distance from the interface for a fluid with smaller Pr number. For the fluid with larger Pr (100), the viscous boundary layer is thicker, and a longer distance is needed for the normal velocity to approach the inviscid value. The normal-velocity gradient is much larger near the interface for the case of smaller Pr number indicating that for such a fluid, the convective heat transfer is more important as compared to the case of a fluid with larger Pr. The main conclusion is that the rate of solidification during stagnation flow is more affected by convection in the case of a fluid with smaller Pr number.

7.4.2. *Effect of* St *number*. Figure 8(a) shows the finite-difference prediction of the variation of the dimensionless solid thickness $\tilde{s}$ with τ for different values of the Stefan number for the case of $Pr = \theta_i = a = b = 1$. It can be seen from Fig. 8(a) that $\tilde{s}$ increases with τ, and that there exists an upper limit of $\tilde{s}$ as τ approaches infinity. It can also be observed that this limit is independent of the Stefan number and that $\tilde{s}$ increases faster for larger St. A larger Stefan number indicates higher energy-transfer rate as compared with latent-heat release rate, resulting in a faster solidification rate. Figure 8(b) shows the temperature distributions along the normal direction during the early ($\tau = 0.1$) and late ($\tau = 100$) stages of solidification for cases with different Stefan number. It can be observed that in the early stages of solidification, variations in Stefan number bring about changes in the temperature distribution and the interface location, and a larger Stefan number results in faster growth of the solid front. At very large times, however, the temperature distribution becomes inde-

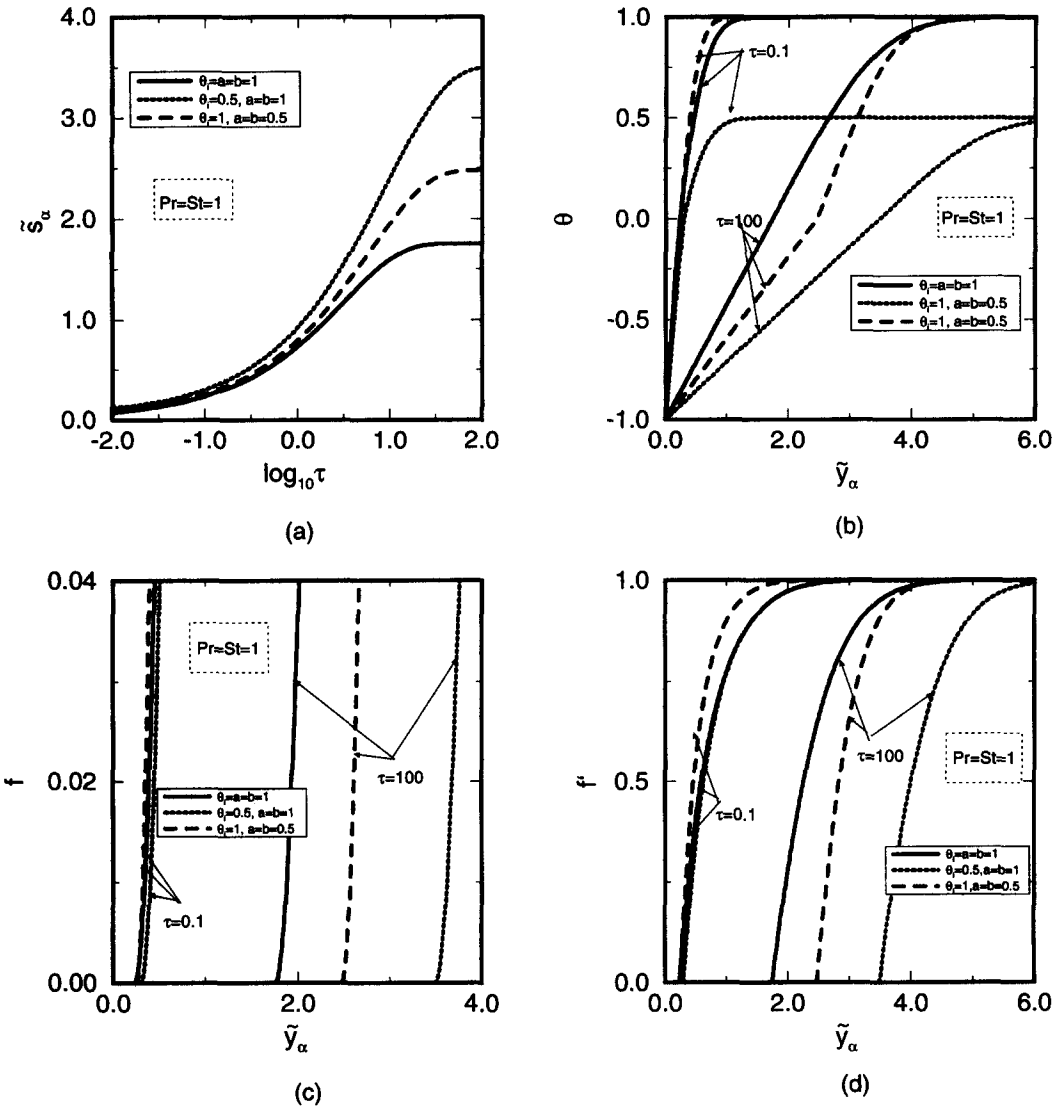

Fig. 9. Comparison of the solidification behavior: effect of θ_i, a and b. (a) solid-front evolution vs time; (b) temperature distributions; (c) velocity distributions; (d) velocity gradient distributions.

pendent of Stefan number. In Fig. 8(c, d), the corresponding normal-velocity distribution and its gradient along the nondimensional normal direction during the early ($\tau = 0.1$) and late ($\tau = 100$) stages of solidification for cases with different Stefan number are shown. The behavior of the velocity distribution is similar to that of the temperature distribution. Variations in Stefan number bring about changes in the velocity distribution in the early stages of solidification. While at a very large time, the velocity distribution becomes independent of Stefan number.

7.4.3. *Effect of* a, b *and* θ_i. Figure 9(a) shows the effect of θ_i, a and b on the solid front growth rate obtained by the finite-difference solution. The dimensionless thickness $\tilde{s}$ increases faster for smaller a, b and θ_i. For the cases with smaller a, b or θ_i, less heat is transferred from the liquid to the solid phase through the interface, so that solidification occurs more rapidly. Figure 9(b) shows the temperature distribution during the early ($\tau = 0.1$) and late ($\tau = 100$) stages or solidification for cases with different values of θ_i, a and b. It can be seen that during the early stages of solidification and at the same position in the liquid phase, the liquid temperature is lower for higher a and b. In the early stages of solidification, higher a and b means that heat transfer is more rapid in the liquid than in the solid phase, and therefore, the liquid temperature drops to a lower value as compared to a case with lower a and b. However, during the late stages of solidification, the temperature distribution and the solid front location approach their asymptotic limits. For a fixed position in the liquid or solid phase, the temperature θ_l or θ_s is lower for the cases with lower a, b. Thus, it can be concluded that variations in the parameters a and b affect both the initial and the long time behavior of the solution. Corre-

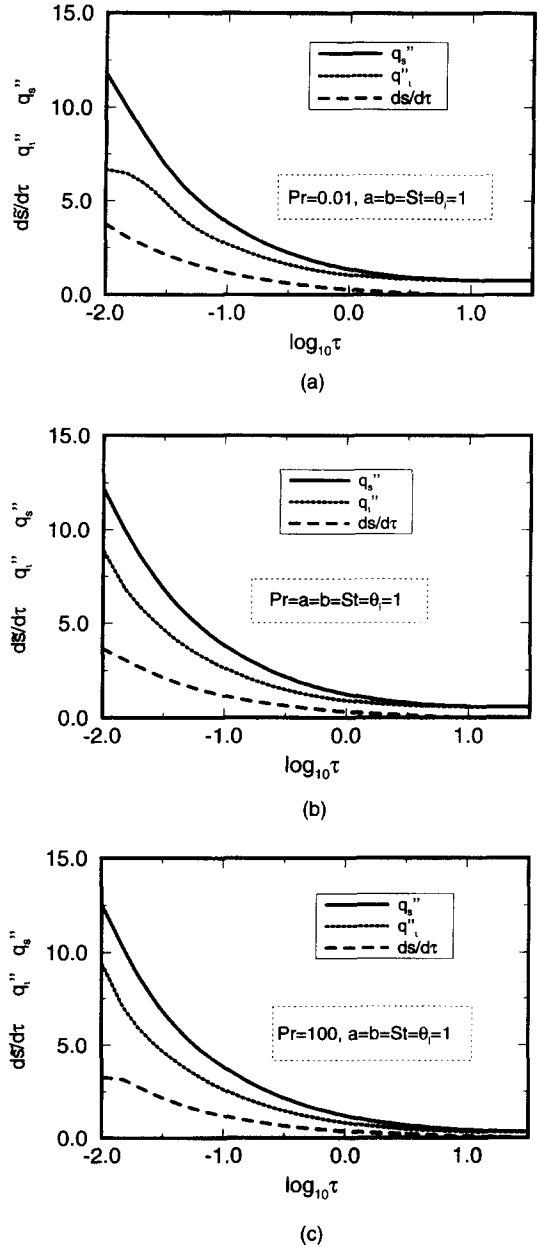

Fig. 10. The time variation of the solid and liquid heat fluxes at the interface and the solid–liquid interface growth rate.

spondingly, Fig. 9(c, d) shows the normal-velocity distribution and its gradient along the dimensionless normal coordinate y_α during the early ($\tau = 0.1$) and late ($\tau = 100$) stages of solidification. It can be concluded that the gradient of the normal-velocity distribution is mainly determined by the Pr of the fluid, while the interface location is affected by several parameters (Pr, a, b and θ_i).

Figure 10(a–c) shows the growth rate of the solid–liquid interface location and the time variation of the heat fluxes at the interface on both the liquid and solid sides for three different Pr numbers (0.01, 1, 100) with $a = b = St = \theta_i = 1$. The existence of a finite asymptotic limit for the solidification front in the stagnation-flow problem may be understood by examining these figures. The fact that the thermal field in the liquid phase approaches a quasi steady behavior in the late stages of solidification implies that the heat flux at the interface on the liquid side decreases not to zero, but to a finite value in the limit of $t \to \infty$. Moreover, the behavior of the heat flux at the interface on the solid side for the stagnation-flow solidification problem is similar to the one in the classical solidification problem. In the classical problem, the solid thickness s increases as $t^{1/2}$ and thus the solid heat flux decreases as $t^{-1/2}$, the same rate of decrease of the liquid heat flux. Since energy arriving at the interface by conduction from the liquid must ultimately be conducted through the solid into the substrate, the solid heat flux must be at least as large as the liquid heat flux. In the stagnation-flow solidification problem, the solid front can only rise to a height which results in a solid-phase heat flux equal to the liquid-phase heat flux. No further solidification is possible after this point.

7.5. *Solidification of water and aluminum*

Some calculations involving the solidification process of water and aluminum using the finite-difference method are discussed next. The time-evolution of the solid front is shown in Fig. 11, where a comparison of the solid-front growth with time corresponding to different strain rates is made. Values of the other relevant parameters are included in the figure. For water [Fig. 11(a)], the cold substrate temperature is set at 20 K below the melting temperature and the initial liquid temperature is chosen as 20 K above the melting temperature. The parameters a, b and Pr are determined by calculating the liquid state properties at $T = (T_i + T_m)/2$ and the solid state properties at $T = (T_o + T_m)/2$. The Neumann solution of the stagnant solidification model (Stefan problem) is also shown in the figure. It can be observed that as time increases, the solid-front location approaches an upper limit for the stagnation-flow solidification model, while in the case of stagnant solidification model, the solid front grows indefinitely with time. A higher value of the strain rate corresponds to a lower upper limit of the solid-front location, which indicates that the effect of the convective heat transfer becomes more important. On the other hand, it can be seen that the time-evolution of the solid-front of the stagnation-flow solidification problem approaches the Neumann solution as the liquid-flow strain rate approaches zero. Similar behavior can be observed in Fig. 11(b) for the stagnation-flow solidification of aluminum. In the calculation, the initial liquid temperature is 100 K above its melting temperature and the cold substrate temperature is 300 K. The parameters a, b and Pr are calculated in the same way as indicated in reference to Fig. 11(a). The range of values for the flow strain rate A is chosen in reference to its magnitude in high-speed spray deposition process for which A is of the

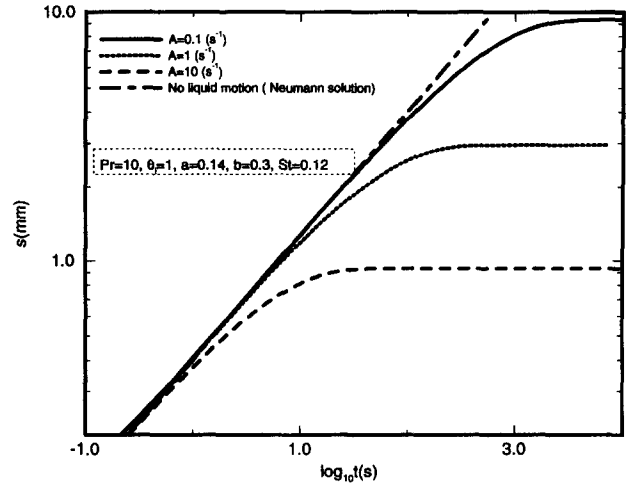

(a)

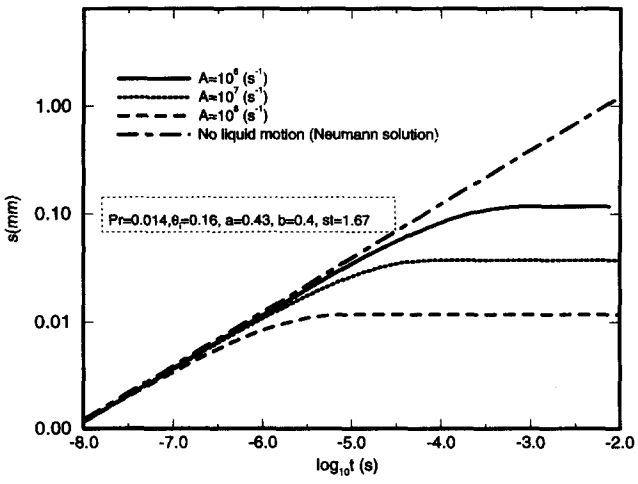

(b)

Fig. 11. Comparison of the solid-front time evolution between the stagnation-flow solidification model and the Neumann solution of the classical Stefan problem, (a) water, (b) aluminum.

order of v/D, where v is the liquid droplet impinging velocity, and D is the droplet diameter.

8. CONCLUSIONS

The viscous stagnation-flow Stefan solidification problem has been defined and a quasi-steady approximation, an instantaneous-similarity method as well as a finite-difference method have been used to solve it and to obtain the solid- and liquid-phase temperature distribution, the liquid-phase velocity distribution, and the interface location. With the use of the quasi-steady approximation, a solution of the problem valid for the final stages of solidification is obtained. Furthermore, by applying the method of instantaneous similarity, the temperature field, the solid–liquid interface position and its growth rate valid for the initial stages of solidification are obtained. Based on the semi-analytical solutions obtained above, the stagnation-flow solidification problem is solved numerically by a finite-difference method after a coordinate transformation to a fixed domain. The Crank–Nicolson method is applied to obtain the finite-difference form of the liquid-phase momentum equation, the liquid- and solid-phase energy equations, and the resulting difference equations are solved by the TDMA method. The location of the liquid–solid interface is obtained by solving the interface energy balance equation coupled with the solid and liquid phase energy equations, as well as the liquid phase momentum equation. To avoid the singularity of the system of equations at the starting time, the instantaneous similarity solution at some sufficiently-small time is used to initiate the finite-difference iteration.

Comparisons of the finite-difference solution with the instantaneous similarity solution as well as with the quasi-steady solution of the velocity field, temperature distribution and solid phase thickness at different times show that in the initial stages of solidification, the finite-difference method and the instantaneous similarity method yield very similar solutions, while the quasi-steady method overpredicts the growth of the solid front. At intermediate times, only the finite-difference solution is accurate. At very large time, the three methods converge to the same solution. All three methods are used to show that the solidification front grows asymptotically to a finite maximum value as time goes to infinity. Parametric studies indicate that for very small Prandtl number ($Pr < 0.01$), the behavior of the solid-front evolution is very close to the result obtained with the inviscid stagnation-flow solidification model [17, 18].

Acknowledgements—This work has been supported by a grant from the National Science foundation (CTS-9224856). Useful discussions with Dr J.-P. Delplanque and Mr S. Ji are acknowledged.

REFERENCES

1. J. Stefan, Uber die theorie der eisbildung, insbesondere uber die eisbildung in polarmaere, *A. Phys. Chem.* **42,** 269–286 (1891).
2. J. C. Muehlbauer and J. E. Sunderland, Heat conduction with freezing or melting, *Appl. Mech. Rev.* **18,** 951–959 (1965).
3. L. E. Goodrich, Efficient numerical technique for one dimensional thermal problems with phase change, *Int. J. Heat Mass Transfer* **21,** 615–621 (1978).
4. A. Y. Belekii and S. N. Zolotarev, Theoretical analysis of fluid dynamics and heat transfer in the single roller rapid solidification method, *Int. J. Rapid Solidificat.* **6,** 51–54 (1991).
5. M. Epstein and F. B. Cheung, Complex freezing-melting interfaces in fluid flow, *A. Rev. Fluid Mech.* **15,** 293–319 (1983).
6. E. M. Sparrow, J. W. Ramsey and S. Harris, The transition from natural convection controlled freezing to conduction controlled freezing, *J. Heat Transfer* **103,** 7–13 (1981).
7. M. Lacroix, Computation of heat transfer during melting of a pure substance from an isothermal wall, *Numer. Heat Transfer B* **15,** 191–210 (1989).
8. G. H. Yeoh, M. Behnia, G. De Vahl Davis and E. Leonardi, A numerical study of three-dimensional natural convection during freezing of water, *Int. J. Numer. Meth. Engng* **30,** 899–914 (1990).
9. Curtic M. Oldenburg and Frank J. Spera, Hybrid model for solidification and convection, *Numer. Heat Transfer B* **21,** 217–229 (1992).
10. L. Hadji and M. Schell, Interfacial pattern formation in the presence of solidification and thermal convection, *Phys. Rev. A* **41,** 863–873 (1990).
11. G. S. Hanumanth, Solidification in the presence of natural convection, *Int. Commun. Heat Mass Transfer* **17,** 283–292 (1990).
12. G. Trapaga, E. F. Matthys, J. J. Valencia and J. Szekely, Fluid flow, heat transfer, and solidification of molten metal droplets impinging on substrates: comparison of numerical and experimental results, *Metall. Trans. B* **23B,** 701–718 (1992).
13. C. San Marchi, H. Liu, E. J. Lavernia and R. H. Rangel, Numerical analysis of the deformation and solidification of a single droplet impinging onto a flat substrate, *J. Mater. Sci.* **28,** 3313–3321 (1993).
14. T. Watanabe, I. Kuribayashi, T. Honda and A. Kanzawa, Deformation and solidification of a droplet on a cold substrate, *Chem. Engng Sci.* **47,** 3059–3065 (1992).
15. H. Liu, E. J. Lavernia and R. H. Rangel, Numerical simulation of substrate impact and freezing of droplets in plasma spray processes, *J. Phys. D: Appl. Phys.* **26,** 1900–1908 (1993).
16. H. Liu, E. J. Lavernia and R. H. Rangel, Numerical investigation of micropore formation during substrate impact of molten droplets in plasma spray processes, *Atomiz. Sprays* **4,** 369–384 (1994).
17. R. H. Rangel and X. Bian, The inviscid stagnation-flow solidification problem, *Int. J. Heat Mass Transfer* **39**(8), 1591–1602 (1996).
18. R. H. Rangel and X. Bian, Numerical solution of the inviscid stagnation-flow solidification problem, *Numer. Heat Transfer A* **28,** 589–603 (1995).
19. K. Brattkus and S. H. Davis, Flow induced morphological instabilities: stagnation-point flows, *J. Crystal Growth* **89,** 423–427 (1988).
20. H. S. Carslaw and J. C. Jaeger, *Conduction of Heat in Solids* (2nd Edn) p. 283. Clarendon Press, London (1959).
21. F. M. White, *Viscous Fluid Flow* (2nd End), p. 153. McGraw-Hill, New York (1991).
22. S. V. Patankar, *Numerical Heat Transfer and Fluid Flow* (1st Edn), pp. 52–54. McGraw-Hill, New York (1980).